



Systematic study of a thulium-doped all-polarization maintaining modelocked fiber laser from a low to high fundamental repetition rate

C. CUADRADO-LABORDE,^{1,2,3,*}  H. MUÑOZ-MARCO,⁴
P. PÉREZ-MILLÁN,⁴ A. DÍEZ,¹  J. L. CRUZ,¹ E. SILVESTRE,⁵ 
AND M. V. ANDRÉS¹ 

¹Departamento de Física Aplicada y Electromagnetismo, ICMUV, Universidad de Valencia, C/ Dr. Moliner 50, Burjassot 46100, Valencia, Spain

²Instituto de Física Rosario (CONICET-UNR), Blvr. 27 de Febrero 210bis, S2000EZZ, Rosario, Argentina

³Pontificia Universidad Católica Argentina, Facultad de Química e Ingeniería, Av. Pellegrini 3314, S2002QEO Rosario, Santa Fe, Argentina

⁴FYLA LASER SL, Ronda Guglielmo Marconi 14, Paterna 46980, Valencia, Spain

⁵Departamento de Óptica, ICMUV, Universidad de Valencia, Dr. Moliner 50, Burjassot E-46100, Spain
*christiancuadrado@uca.edu.ar

Abstract: In this work, we present an experimental and theoretical study of a passively modelocked all-fiber laser that fully retains polarization with a fundamental repetition rate ranging from 0.1 to 1 GHz. The whole cavity consists of a highly-Tm-doped fiber in tandem with a passive fiber, both with polarization-maintenance, with a dichroic mirror on one end and a semiconductor saturable absorber mirror on the other. We experimentally characterized the output of this laser, which emits a train of transform-limited sub-picosecond light pulses around the two microns. The high stability of this laser was also experimentally verified. Together with this, a detailed theoretical model was developed, confirming the experimental results.

© 2025 Optica Publishing Group under the terms of the [Optica Open Access Publishing Agreement](#)

1. Introduction

High repetition rate modelocked fiber lasers have drawn significant interest recently due to their widespread applications in science and industry, including all-optical buffering [1], astronomical spectroscopy [2], biophotonics [3], optical arbitrary waveform generation [4], and thermal damage-free material removal [5]. Although solid-state lasers operating at multi-gigahertz have shown effectiveness [6], fiber lasers unquestionably provide distinct benefits such as exceptionally small size, superior thermal control, and stability. In particular, these fiber lasers operating with emission wavelengths around the eye-safe two micrometer region show considerable potential for applications such as LIDAR [7], photonic analog-to-digital conversion [8], welding of polymers [9], low-latency high-speed hollow-core fiber-optic links [10], and free-space communication [11]. Passive mode-locking at the fundamental repetition rate in ultra-short Fabry–Perot fiber cavities has been shown to be a more scalable, compact, and reliable technique of generating femtosecond pulses at repetition rates in the gigahertz range, than other alternatives such as active mode-locking [12], or harmonic mode-locking [13]. Among them, the generation of pulses using semiconductor saturable absorbers mirrors (SESAM) presents several notable advantages over alternative methods, such as nonlinear phase shift. These techniques include Kerr-lens mode-locking [14], nonlinear polarization rotation [15], and methods that utilize intensity-dependent frequency conversion, such as nonlinear mirror mode-locking [16]. The efficacy of these approaches relies on the nonlinear dynamics triggered by high-intensity light pulses, which affect the gain and loss experienced by light pulses during their round-trips,

allowing the system to function as an artificial saturable absorber. Although these techniques can produce extremely short pulses, they often face stability issues due to environmental thermal variations and generally exhibit reduced self-starting capabilities; not to mention the impossibility to scale some of these techniques into ultra-short cavities.

Among the more recently modeled fiber laser sources in the two micrometer range emitting at high fundamental repetition rates, we can mention the Tm/Ho-doped laser with a mixed bulk optics/fiber optics configuration presented in Ref. [17]; and also the thulium-doped all-fiber configuration with double cladding presented in Ref. [18]. Later, the same team from Ref. [18] increased the repetition rate up to the gigahertz range with the same configuration as before, except that the medium gain was replaced by a TDF [19]. Tang et al. exceed the fundamental repetition rate of 4 GHz by using a custom-made Tm³⁺/Ho³⁺ active fiber [20,21]. In the same direction, a mode-locked fiber laser with a repetition rate slightly above 1 GHz and low noise was demonstrated by using a specially designed Tm³⁺-doped barium gallo-germanate fiber with reduced dispersion in Ref. [22]. Recently, Liang et al. demonstrated a high-power fiber laser system that delivers femtosecond pulses with a fundamental frequency above 10 GHz [23]. Later, the same team achieved high power pulses with a fundamental frequency of 1 GHz by using a multistage fiber amplifier and a nonlinear pulse compressor [24]. Finally, we could mention also the work presented in Ref. [25], where an interesting analysis was made of the different regimes in this type of lasers with very short fiber cavities.

We very recently proposed a polarization-maintaining passively modelocked all-fiber laser with a fundamental repetition rate of 1 GHz [26]. Our first purpose here is analyzing the evolution of this polarization-maintaining (PM) passively modelocked all-fiber laser when the fundamental repetition rate increases from 0.1 to 1 GHz. While our second purpose is to develop in detail a comprehensive theoretical model, whose numerical results will be contrasted with the experimental measurements.

2. Experimental

2.1. Setup

In Fig. 1 we show the experimental setup, the PM oscillator consisted of a Fabry-Perot (FP) resonator that fully preserves polarization. This resonator is pumped by a CW laser emitting at 1561 nm, with a maximum power of 800 mW. The pump power entered the FP cavity via a dichroic filter deposited on a fiber pigtail ferrule (transmissivity > 90% at 1561 nm, reflectivity ~99% for optical wavelengths higher than 1780nm), see its transmittance curve T_d in Fig. 2(a). This fiber pigtail is composed of a highly doped (~7%) PM TDF (PM-TSF-5/125, Panda-Type Tm-Doped optical fiber by Nufern, numerical aperture 0.24, operating wavelength 1900-2100 nm, and 362 dB/m absorption at 1560 nm) terminated in a FC/PC connector (fiber connector with physical contact) in one end and a free end in the other. The emission cross section σ_e for a highly-doped TDF can be seen in Fig. 2(a) [27]. In general, except otherwise specified, the remaining extreme of the PM TDF pigtail was fusion spliced to a second delay line fiber pigtail (PM1550-XP by Nufern, numerical aperture 0.125, cutoff wavelength of 1380 ± 60 nm, and ≤ 1 dB/m loss at 1550 nm). The FP cavity was closed by facing a SESAM (BATOP, central wavelength operation 1960nm, absorbance 30%, and relaxation time constant 10 ps) to the fiber ferrule of the PM delay line pigtail. The measured reflectance and group delay dispersion (GDD) for the SESAM are shown in Fig. 2(b) [28]. The output of this laser is obtained through a PM wavelength division multiplexer which is located outside the FP cavity (WDM, 1550/1950nm, insertion loss: pass to common < 0.6 dB at 1950nm and reflection to common < 0.5 dB at 1550 nm); which in turn is connected to a PM fiber optic coupler (PM OFC, 90/10, central wavelength 1950nm and fast axis blocked), where a PM optical isolator was also included to avoid unwanted reflections to the cavity (PM I, central wavelength of 1950 ± 20 nm, and peak isolation of 28 dB, and insertion loss of 0.6 dB). Additionally, we included in the output FC/APC connectors (fiber

10 GHz electrical spectrum analyzer (resolution ≥ 1 Hz). Finally, the average output power was measured with a pyroelectric sensor with real-time and storage acquisition capabilities.

2.2. Results and discussion

In Fig. 3, the different optical spectra obtained can be observed by using different combinations of active optical fiber lengths of PM TDF (LTDF) and passive delay lengths of PM-1550XP (LDL). Therefore, we begin our experimental description with a configuration that utilizes 200 mm of PM TDF and 640 mm of PM-1550XP optical fiber lengths. This results in a total cavity length (LT) of 840 mm, which in turn produced a train of single light pulses at the fundamental repetition rate of $f = 121$ MHz for a pump power of 145 mW, measured at the input of the dichroic filter. The spectrum of the stable light pulse train has an emission peak at 2050nm with an optical bandwidth of 2.23 nm, see Fig. 3(a). In the following configuration, we shortened the cavity up to 420 mm in length by combining 200 mm of PM TDF with 220 mm of PM-1550XP optical fiber lengths. This in turn produced a stable light pulse train at the fundamental repetition rate $f = 244$ MHz for a pump power of 200 mW. In this case, the optical spectral profile width was 5.4 nm, centered at 2054nm; see Fig. 3(b). Next, we shortened further the cavity by using 130 mm of PM TDF plus 90 mm of PM-1550XP optical fiber lengths. This resulted in a total cavity length of 220 mm, which in turn produced a train of single light pulses at the fundamental repetition rate of $f = 464$ MHz for a pump power of 247 mW. The optical spectral profile can be observed in Fig. 3(c), with a spectral width of 2.7 nm centered at 1968nm. As compared with the previous measurements, it is evident the spectral blueshift of ~ 90 nm. However, it should be emphasized that there is not any component within the resonator performing an ad-hoc filtering in the cavity, and thereby fixing in this way the emission wavelength, except by the interplay of the optical bandwidths of the medium gain and the reflectivity of the SESAM. By shortening further the cavity to reach a cavity length of 196 mm (120 mm of PM TDF plus 76 mm of PM-1550XP optical fiber lengths), we obtained a fundamental repetition rate $f = 521$ MHz for a pump power of 258 mW. This optical spectral profile can be observed in Fig. 3(d), with a FWHM of 8.5 nm and an emission wavelength of 1951nm. Next, we shortened one more time the cavity by adding to the 120 mm length of PM TDF a 36 mm long of PM 1550-XP delay line. Therefore, the output light pulses had a fundamental repetition rate of 654 MHz when the pump power was of 262 mW. The optical spectrum profile can be observed in Fig. 3(e), where the measured FWHM was of 2.1 nm. Finally, we decided to preclude of the delay line, just by using a cavity entirely composed of the PM TDF. This cavity was previously designed by us, since it is necessary not just using a PM TDF pigtail, but an entire PM TDF cavity with two fiber ferrules in each end, in one of them it was deposited the dichroic filter, as we did previously, and at the other a fiber ferrule, which was confronted to the SESAM. Thus, the cavity length was just of 106 mm of PM TDF; the resonator is then reduced to an extremely compact, robust and low-loss cavity of PM TDF. We can see in Fig. 3(f) the optical spectrum profile centered at 1961nm, with a spectral width of 7 nm. Finally, it can be observed a noticeable spectral shift for the emission wavelength between different cavity configurations. This emission wavelength is determined by the interplay of numerous cavity parameters in each configuration and cannot be precisely regulated without the use of an intracavity bandpass filter. Unfortunately, the ultra-short dimensions of the cavities preclude or limit this option. However, it is still possible to control the emission wavelength by carefully selecting the cut-off wavelength of the dichroic filter and the spectral dependence of the SESAM's reflectivity in order to limit this zone to a narrower range.

As an illustration of the temporal characterization of the laser system under study, the pulse train operating at a repetition rate of 521 MHz is depicted in Fig. 4(a) together with its corresponding RF spectrum. A thorough 4-hour continuous operating test without any active temperature management was performed to show the stability of this laser. As can be seen from the data in Fig. 4(b), the output power changes throughout this time were remarkably small, with a standard

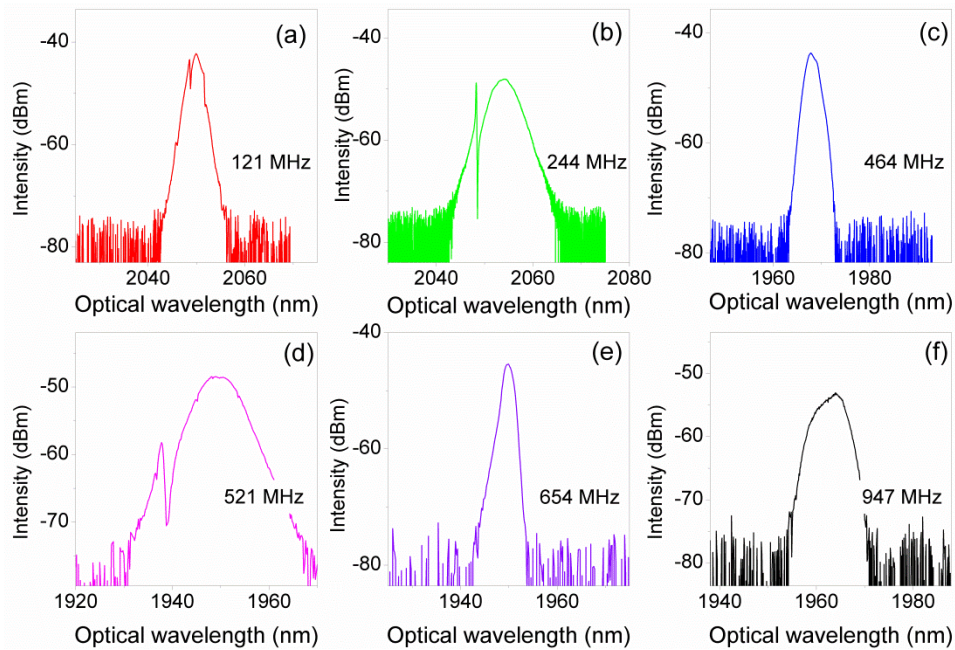


Fig. 3. Optical spectra at different fundamental repetition rates: (a) 121 MHz, (b) 244 MHz, (c) 464 MHz, (d) 521 MHz, (e) 654 MHz, and (f) 947 MHz.

deviation of only 1.15%. The idea of strong temporal stability was further supported by an eye pattern analysis that showed clear characteristics such as narrow amplitude crossings at the half-intensity level, which are a sign of minimal temporal jitter (see the red arrows in the inset of Fig. 4(b)). This remarkable stability in the optical light train is a key characteristic inherently shared among all PM fiber lasers [30]. Interestingly, the light pulses generated by the laser oscillator were so narrow that they exceeded the detection capabilities of conventional measuring tools such as oscilloscopes or auto-correlators due to their limited energy. While optical amplification was considered as a potential alternative, it was dismissed due to concerns about altering the original pulse waveform. Thus, a less-invasive approach was adopted, involving measuring the pulse broadening caused by a known dispersion effect [31]. This data was then used to accurately calculate the required pulse width at the input of the dispersive line to align with the actual dispersed profile. For this purpose, a specific optical fiber (Corning LEAF, with a numerical aperture of 0.14) measuring 210 meters in length was employed to transmit the pulse train from the oscillator. The chromatic dispersion of this fiber at the relevant wavelength was precisely determined by us experimentally using an interferometric technique [32], being 34.15 ps/(nm × km) at 1961 nm. The resulting temporal pulse profile after traversing the 210-meter dispersive line is presented in Fig. 4(c). Additionally, simulations were conducted to model the spread of unchirped sech^2 light pulses under varying temporal widths to achieve alignment with the experimental data. Notably, a temporal width of 0.50 ps at the input of the dispersive line was found to be the best suited to match the measured dispersed light pulse, as illustrated in Fig. 4(c). This alignment is particularly crucial since the laser in question is anticipated to emit a soliton-like pulse characterized by a minimal time-bandwidth product, an inherent property of sech^2 pulses, with a value of 0.315 [33,34]. The previously measured spectral bandwidth of 8.5 nm by the oscillator corresponds to a time-bandwidth product of 0.335, very close to 0.315, thus corroborating, within the expected precision the original hypothesis and experimental findings.

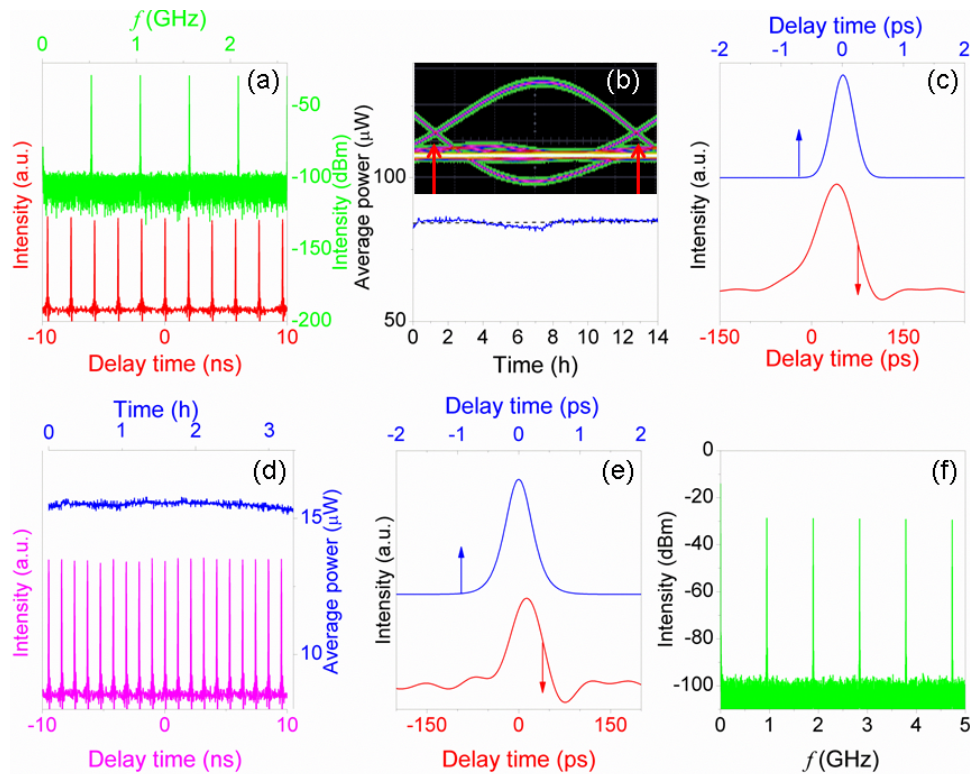


Fig. 4. (a) Optical train and RF spectrum at 521 MHz. (b) Measured average power in long range operation at 521 MHz plus eye pattern at this repetition rate. (c) Oscilloscope trace measured at the output of the dispersive line (red curve, bottom axis), together with pulse profile reconstructed at the output of the oscillator (blue curve, top axis). (d) Optical train at 947 MHz and measured average power in long range operation. (e), same as (c), for a fundamental repetition rate of 947 MHz. (f) RF spectrum at 947 MHz.

As an additional example for illustration, we also present the optical light train achieved at the fundamental repetition rate of 947 MHz, as indicated in Fig. 4(d), corresponding to a pump power of 339 mW. In the same figure, it can be observed the measured average output power under long range operation. In a similar manner to our previous procedure for the fundamental repetition rate of 521 MHz, we conducted measurements to determine the pulse width for this particular configuration. The results are depicted in Fig. 4(e), which exhibits both the pulse measured at the output of the dispersion line and the reconstructed pulse at the output of the oscillator. Specifically, Fig. 4(e) illustrates the temporal pulse profile measured at the output of the dispersive line, revealing a measured FWHM of 54 ps. Furthermore, it includes a simulated transform-limited sech^2 light pulse at the input of the dispersive line, showing a temporal width of 0.53 ps, capable of accurately match the measured dispersed light pulse with the simulated dispersed pulse. Notably, the spectral bandwidth measured at the output of the oscillator was 7 nm, as detailed in Fig. 3(f), leading in conjunction with 0.53 ps to a time-bandwidth product of 0.289, again close to 0.315, aligning with our initial assumptions of chirp-free sech^2 pulses. In Fig. 4(f) it is shown the RF spectrum at the fundamental repetition rate of 947 MHz showing up to the 4th overtone. The sideband suppression in excess of 70 dB is a clear indication of the absence of amplitude modulation instabilities in the output train. Finally, a resume of the main experimental results obtained for each cavity configuration is provided in Table 1, including the

average power P_{avg} measured for each cavity configuration. Additionally, the temporal resolution limit of the photodetectors (> 40 ps) had been exceeded for a few temporal observations at the output of the dispersive line. These measurements were made at fundamental repetition rates of 121, 464, and 654 MHz. A minimal temporal width, denoted by an asterisk, see last column in Table 1, is suggested for each of them by both the spectral bandwidth and solitonic emission. For instance, a light pulse with a FWHM of 2 ps at the input of this dispersive line broadens to ~ 15 ps after a propagation of 210 m long, which is significantly lower than the resolution of the available photodetector. It should be mentioned, on the other hand, that the possibility of propagation longer enough to achieve a higher temporal broadening, was not possible, because at this wavelength the losses are significant and the decrease in the signal-to-noise ratio makes difficult a reliable temporal measurement.

Table 1. Resume of the experimental characterization for each cavity configuration

f	L_{TDF}	L_{DL}	L_{T}	λ_0	$\Delta\lambda$	Δt	P_{avg}
[MHz]	[mm]	[mm]	[mm]	[nm]	[nm]	[ps]	[μW]
121	200	640	840	2050	2.2	$> 2^*$	198
244	200	220	420	2054	5.4	0.70	123
464	130	90	220	1968	2.7	$> 1.5^*$	90
521	120	76	196	1951	8.5	0.50	84
654	120	36	156	1954	2.1	$> 1.9^*$	71
947	106	0	106	1961	7.0	0.53	15

3. Theoretical

3.1. Model

Figure 5 shows the block diagram followed in the numerical model of this laser. The linear cavity scheme is constituted by a segment of gain fiber, a passive fiber or delay line (which is precluded at the highest repetition rate operation of 1 GHz); while a SESAM and dichroic filters were used as cavity end-reflectors. Therefore, the cavity is handled equally to a ring configuration in this model, since any standing-wave effect is neglected.

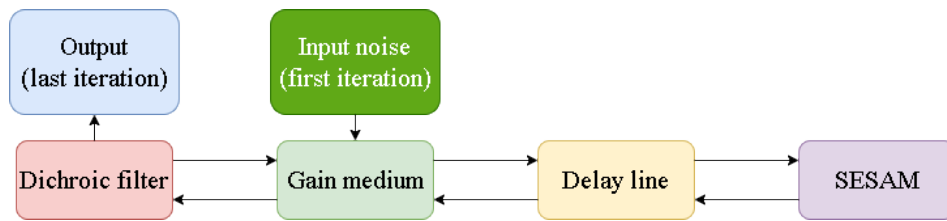


Fig. 5. Block diagram of the laser model.

The generalized scalar nonlinear Schrödinger equation was used to model the pulse propagation through the cavity [35]:

$$\frac{\partial A(z, t)}{\partial z} = -\alpha \frac{A(z, t)}{2} + \int_{-\infty}^{\infty} \frac{g(\omega)}{2} \hat{A}(\omega) e^{-j\omega t} d\omega - j \frac{\beta_{20}}{2} \frac{\partial^2 A(z, t)}{\partial t^2} + j\gamma |A(z, t)|^2 A(z, t), \quad (1)$$

where $A(z, t)$ denotes the complex envelope of the optical pulse, t is the local pulse time measured in a reference frame moving at the same speed as the signal, z is the propagation distance, α is

the linear loss, β_{20} is the GVD, γ is the nonlinear coefficient, $\hat{A}(\omega)$ is the Fourier transform of $A(t)$, $g(\omega)$ is the gain coefficient; and ω is the baseband angular frequency (i.e., $\omega = \omega_{\text{opt}} - \omega_0$, where ω_{opt} is the optical angular frequency and ω_0 is the carrier angular frequency). The gain saturation was considered as:

$$g(\omega) = g_0(\omega) \left[1 + E_S^{-1} \int |A(t)|^2 dt \right]^{-1}, \quad (2)$$

where E_S is the saturation energy of the medium gain, which is usually related to pumping strength, and $g_0(\omega)$ is the unsaturated gain coefficient related to the doping concentration; whose spectral dependence is shown in Fig. 2(a) following the emission cross section σ_e . As it has been demonstrated, raising the pump power simultaneously increases both g_0 and E_S . However, in the simulations, it typically suffices to maintain g_0 at a constant value while adjusting E_S only [36]. Further, since the recovery time of the active medium is much longer than the cavity round-trip time, Eq. (2) represents the gain due to an active medium that is independent of time [37].

On the other hand, the time-dependent absorption of the SESAM can be modeled in two steps [38,39]. In the first step, it is applied the nonlinear part of the saturation loss on the temporal complex envelope of the pulse profile:

$$A(t) \longrightarrow \sqrt{1 - \alpha_S(t)} A(t), \quad (3)$$

where $\alpha_S(t)$ represents the saturable absorption, which in turn is a function of the intensity of the pulse itself, through $\xi(t)$:

$$\alpha_S(t) = \Delta R \exp[-\xi(t)] \left(1 + \tau^{-1} \int^t \exp[\xi(t')] dt' \right). \quad (4)$$

In Eq. (4), ΔR is the modulation depth, while τ is the relaxation time constant, and $\xi(t)$ is defined through:

$$\xi(t) = \int^t (\tau^{-1} + E_{S, \text{SESAM}}^{-1} |A(t')|^2) dt', \quad (5)$$

with $E_{S, \text{SESAM}} = \Phi_S A_A$, where Φ_S and A_A are the saturation fluence and the pulse mode area on the saturable absorber, respectively. Finally, in the second step, on the complex envelope of the Fourier transform of the pulse profile is applied the linear part of the saturation loss plus the delay dispersion of the SESAM:

$$\hat{A}(\omega) \longrightarrow \sqrt{R_{\text{lin}}(\omega)} \exp[j\phi_p(\omega)] \hat{A}(\omega), \quad (6)$$

where $R_{\text{lin}}(\omega)$ is the linear reflectivity (or low intensity spectral reflectance), and $\phi_p(\omega)$ is the phase introduced by the SESAM, by discarding the first two terms of its Taylor series expansion around ω_0 . This phase was calculated by integrating twice $D_2(\omega)$, the GDD of the SESAM:

$$\phi_p(\omega) = \int_{\omega_0}^{\omega} d\omega_1 \int_{\omega_0}^{\omega_1} D_2(\omega_2) d\omega_2. \quad (7)$$

Note that both integrals in Eq. (7) have upper limits that span values both larger and less than ω_0 . Both $R_{\text{lin}}(\omega)$ and $D_2(\omega)$ can be inferred from Fig. 2(b), where they have been represented, but as a function of the optical wavelength λ .

The parameters used in the calculation are shown in Table 2, the corresponding values were rationally selected by referring to the data sheet of the components used in the experimental section (when available); e.g., SESAM and PM 1550-XP, or to very similar components when a

complete data sheet was not found for the specific component used; e.g. PM TDF where we used the data published of a highly-doped TDF, although not PM. A single round-trip is equivalent to the optical field propagating through each part of the resonator in a back and forth fashion following the block diagram sketched in Fig. 5. Before going back to the following iteration, the spectrum of the signal intensity is multiplied by the wavelength-dependent reflectance of the dichroic filter (RD), in order to account for the dichroic action, with $R_D = 1 - T_D$, and T_D the dichroic filter transmittance previously shown in Fig. 2(a). The numerical simulations were performed using the split-step Fourier transform method [40,41]; the program starts by incorporating white noise with one photon per frequency channel as input to the medium gain in the first iteration, while the output is obtained through the dichroic filter in the last iteration, see Fig. 5. Finally, we used a temporal frame of 0.5 ns with points separated by ~ 30 fs.

Table 2. Parameters of the PM Tm-doped Fabry-Perot modelocked fiber laser model

	Parameter	Value	Units
Dichroic mirror	R_D	$R_D(\omega) = 1 - T_D(\omega)$, For $T_D(\omega)$, see Fig. 2(a)	unitless
Delay line	β_{20}	-76	ps ² /km
	γ	1.5×10^{-3}	W ⁻¹ m ⁻¹
	L_{DL}	from 0 (for $f = 947$ MHz) to 0.64 (for $f = 121$ MHz)	m
Gain medium	g_0	$g_0(\omega) = 64\sigma_e(\omega)/\max(\sigma_e)$ for $\sigma_e(\omega)$, see Fig. 2(a)	m ⁻¹
	L_{TDF}	from 0.2 (for $f = 121$ MHz) to 0.106 (for $f = 947$ MHz)	m
	β_{20}	-20	ps ² /km
	γ	0.8×10^{-3}	W ⁻¹ m ⁻¹
	E_s	from 0.2 (for $f = 121$ MHz) to 2 (for $f = 947$ MHz)	pJ
SESAM	ΔR	0.18	unitless
	Φ_{sat}	0.65	J/m ²
	A_{sat}	19.63	μm^2
	τ	10	ps
	R_{lin}	$R_{lin}(\omega)$, see Fig. 2(b) for $R_{lin}(\lambda)$	unitless
	D_2	$D_2(\omega)$, see Fig. 2(b) for $D_2(\lambda)$	fs ²

3.2. Numerical results and discussion

In general, two thousand roundtrips are more than enough to achieve a stable emission. We discovered through the experiments that a stable emission could be achieved for a range of pump powers, instead of for a single value. In this simulation, the pump power was represented by the saturation energy E_s of the medium gain, as we previously discussed; see Eq. (2). We choose the cavity configuration at the fundamental repetition rate of 521 MHz as an example, then $L_{TDF} = 120$ mm and $L_{DL} = 76$ mm in the simulation, according to the experimental section. In this case, a stable single-pulse emission was achievable whenever $0.2 \text{ pJ} \leq E_s \leq 16 \text{ pJ}$. In this range, the temporal and spectral pulse widths varied correspondingly as a function of E_s . The higher the saturation energy, the narrower the pulse profile in the time domain, the wider the spectral profile, and the longer the central emission wavelength. This range defines the boundaries

within which stable emissions can be achieved while also showcasing the relationship between temporal and spectral characteristics under different pump powers at this specific repetition rate. At the lowest saturation energy ($E_s = 0.2$ pJ), the output light pulse has a $\Delta t = 2.5$ ps and $\Delta\lambda = 3$ nm (centered at 1902nm), while at the highest saturation energy ($E_s = 16$ pJ), the output light pulse has a $\Delta t = 0.23$ ps and $\Delta\lambda = 20$ nm (centered at 1923nm), in both cases measured at the FWHM. The temporal waveform and the spectral profile at three representative saturation energies are shown in Figs. 6(a) and 6(b), respectively; in both cases normalized to unity for comparison purposes. We discovered that at saturation energies below the threshold ($E_s < 0.2$ pJ), it was only possible to align multiple sub-pulses over a noisy background rather than a single clean pulse. Higher saturation energies ($E_s > 16$ pJ), on the other hand, produced an output of multiple, irregularly spaced pulses pattern over a well-resolved clean background. The output light pulses were confirmed to be solitonic of sech^2 profile and transform-limited, especially as the saturation energy approached the maximum permissible value for single-pulse emission. As an example, for $E_s = 5.8$ pJ, the time domain waveform has a FWHM of 0.5 ps; while the optical spectrum show a FWHM of 8 nm; see Figs. 6(a) and 6(b), respectively. On the other hand, our experimental results at this fundamental repetition rate of 521 MHz were $\Delta t = 0.5$ ps and $\Delta\lambda = 7.2$ nm; see Figs. 3(d) and 4(c), which is very close to these values. Notably, the absence of sidebands in the optical spectrum for the numerical results was also confirmed by the experimental measurements. This typically occur when the soliton period is less (or comparable) to the cavity length, with spectral sidebands lying outside the gain band of the active fiber [42]. Despite the overall consistency between the experimental results and this theoretical model, a discrepancy is observed in the spectral shift of the emission. Specifically, this divergence is seen in the shift from the experimentally measured central wavelength of 1961nm to the calculated 1920nm; see Figs. 3(d) and 6(b). It is hypothesized that this variation may stem from the uncertainty surrounding $g_0(\omega)$, prompting the utilization of an alternative value from literature sources that pertains to a similar TDF fiber of similar dopant concentration, although not PM. Figure 6(c) shows the build-up in the time-domain at the repetition rate of 521 MHz and using $E_s = 5.8$ pJ; after the first ~ 700 round-trips the pulse preserves its final form. In this case, the amplitude fluctuations are less than 0.2% after the 700th roundtrip, in contrast to the train obtained at lower saturation energies, which has high amplitude fluctuations of 5% when $E_s = 0.2$ pJ. This amplitude fluctuation lasted indefinitely at low saturation energies and did not decrease over time. The same effect has been observed experimentally at equivalently low pump powers once the lasing threshold is passed, but it can be significantly reduced by correctly adjusting the pump power to a higher setting.

As a second example, we consider the cavity configuration at a fundamental repetition rate of 947 MHz, with $L_{\text{TDF}} = 106$ mm and $L_{\text{DL}} = 0$ mm in the simulation, as shown in the experimental section. A stable single-pulse emission was achieved when E_s ranged from 0.3 to 7 pJ. As expected, and similarly to the preceding example, the temporal and spectral pulse widths varied as a function of E_s in the same way. At the lowest saturation energy ($E_s = 0.3$ pJ), the output light pulse has a $\Delta t = 0.98$ ps and $\Delta\lambda = 5$ nm (centered at 1904nm), whereas at the maximum saturation energy ($E_s = 7$ pJ), the output light pulse has a $\Delta t = 0.28$ ps and $\Delta\lambda = 16$ nm (centered at 1923nm), both measured at the FWHM. Figures 6(d) and 6(e) illustrate the temporal waveform and spectral profile at three representative saturation energies, respectively, with both normalized to unity for comparison. The output light pulses were again confirmed to be solitonic of sech^2 profile and transform-limited. As an example, for $E_s = 2$ pJ, the time domain waveform has a FWHM of 0.57 ps; while the optical spectrum has an FWHM of 7.8 nm centered at 1906nm; see Figs. 6(d) and 6(e), respectively. Our experimental results at this fundamental repetition rate of 947 MHz were $\Delta t = 0.55$ ps and $\Delta\lambda = 8.5$ nm; as shown in Figs. 3(f) and 4(e), which are very near to these values. Finally, Fig. 6(f) shows the minimum temporal pulse width for single-pulse emission per round-trip and its corresponding spectral pulse width as a function of the fundamental

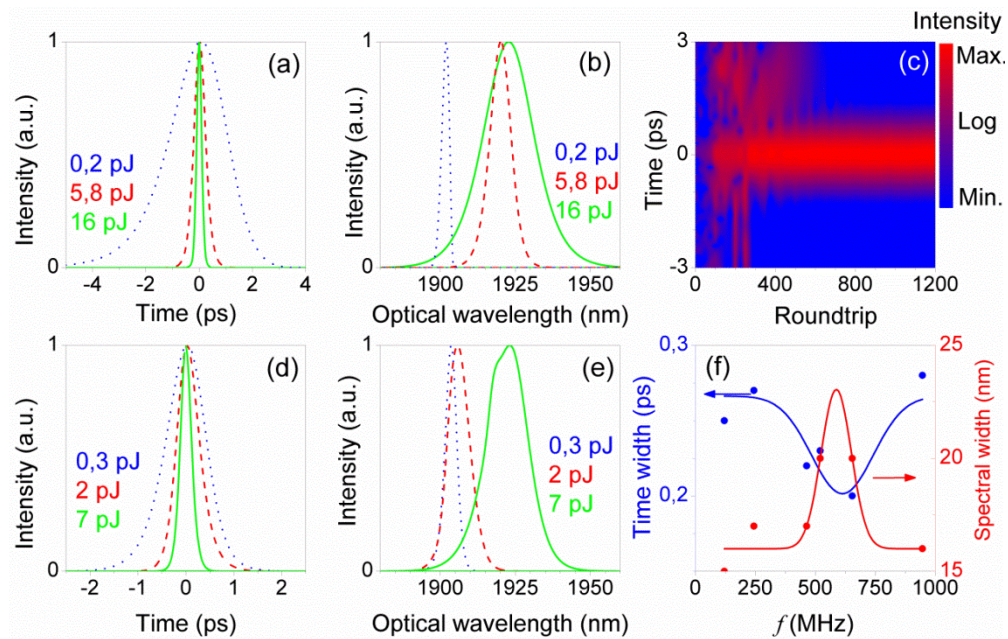


Fig. 6. Numerical simulation at the fundamental repetition rate of 521 MHz: (a) temporal waveform, and (b) optical spectrum at the two thousandth roundtrip for three different saturation energies $E_s = 0.2, 5.8,$ and 16 pJ. (c) Build-up in the time-domain for the fundamental repetition rate of 521 MHz and $E_s = 5.8$ pJ. Numerical simulation at the fundamental repetition rate of 947 MHz: (d) temporal waveform, and (e) optical spectrum at the two thousandth roundtrip for three different saturation energies $E_s = 0.3, 2,$ and 7 pJ. (f) Minimum temporal pulse width for single-pulse emission (blue dots) and its corresponding spectral pulse width (red dots) as a function of the fundamental repetition rate (the solid curves are just a guide to the eyes).

repetition rate. These results were always obtained at the maximum saturation energy possible for stable single-pulse emission for each cavity configuration; and have been obtained from Table 3. Interestingly, the minimum pulse width is obtained for a cavity whose fundamental repetition rate is ~ 500 MHz. This result was confirmed by our experimental measurements, where the light pulses at 521 MHz were narrower than at 947 MHz; and is also in line with previous theoretical works [43,44]. Table 3 completes this characterization by including these numerical results together with its counterpart: the pulse characteristics at the minimum saturation energy possible for stable single-pulse emission. Additionally, we have also included the calculation of the time-bandwidth product and the central emission wavelength. It is worth to mention that the experimental results presented in the preceding section for each cavity configuration are within these limits founded numerically, see Table 1. Further, as the simulations also showed a similar behavior at high saturation energies, the existence of the peak at short wavelengths in the spectra of Figs. 3(a), 3(b), and 3(d) would be the result of an excess of pump power.

To conclude this section, we performed a numerical study to evaluate the possibility to attain larger repetition rates using this configuration, in the range 1-5 GHz. This investigation is crucial because we want to understand the constraints and potential inherent in our current setup. The entire cavity was essentially a simple segment of the same heavily doped TDF used before. In this case, it was also necessary to decrease the temporal frame to 0.15 ns. We performed a similar analysis to that provided in Table 3 to find the minimum and maximum saturation energies required for steady-state single-pulse emission; Table 4 summarizes these results. We

Table 3. Pulse parameters for single-pulse emission at minimum and maximum saturation energy E_s at each cavity configuration

f	L_{TDF}	L_{DL}	L_T	E_s	Δt	$\Delta\lambda$	TBP	λ_0
[MHz]	[mm]	[mm]	[mm]	[pJ]	[ps]	[nm]	Unitless	[nm]
121	200	640	840	0.1	7.5	1	0.616	1911
				10	0.25	15	0.304	1923
244	200	220	420	0.1	4.6	2	0.758	1907
				10	0.27	17	0.373	1922
464	130	90	220	0.2	2.89	3	0.72	1900
				13	0.22	17	0.304	1922
521	120	76	196	0.2	2.5	3	0.622	1902
				16	0.23	20	0.373	1923
654	120	36	156	0.2	1.98	4	0.657	1901
				14	0.2	20	0.324	1923
947	106	0	106	0.3	0.98	5	0.405	1904
				7	0.28	16	0.363	1923

start by 1 GHz, as expected, the results were very close from those obtained at 947 MHz, see Table 3. On the other hand, when the cavity is reduced to achieve higher fundamental repetition rates, the required saturation energy range first drops to 2 GHz, then grows continuously as the fundamental repetition rate increases. From an experimental point of view, the probability of SESAM damage doubles at high repetition rates, since not only is a higher pumping power required, but the cavity must also be shortened. Thus, the pumping power reaching the SESAM increases twofold. Finally, it is worth to emphasize that the results reported in Table 4 for Δt and $\Delta\lambda$ are in line with previous high fundamental repetition rate TDF lasers whose fundamental repetition rate > 1 GHz; e.g., Ref. [23].

Table 4. Pulse parameters for single-pulse emission at minimum and maximum saturation energy E_s from 1 GHz to 5 GHz

f	L_{TDF}	L_{DL}	E_s	Δt	$\Delta\lambda$	TBP	λ_0
[GHz]	[mm]	[mm]	[pJ]	[ps]	[nm]	Unitless	[nm]
1	103	0	0.3	0.96	5	0.397	1904
			8	0.24	16	0.311	1923
2	51	0	0.3	1.43	3	0.351	1914
			5	0.36	10	0.294	1917
3	34	0	0.3	1.17	3	0.286	1916
			11	0.32	12	0.313	1918
4	26	0	0.4	1.18	3	0.289	1916
			15	0.31	14	0.354	1918
5	21	0	0.7	1.17	4	0.382	1916
			17	0.45	11	0.404	1917

4. Conclusions

In this study, we presented a detailed exploration of a full PM passively modelocked all-fiber laser operating within a fundamental repetition rate range from 0.1 to 1 GHz. The laser system

comprises a highly-Tm-doped fiber along with a passive optical fiber incorporating a SESAM at one termination and a dichroic mirror at the other. The laser generates a series of transform-limited sub-picoseconds light pulses around two microns. Furthermore, the robust stability exhibited by this laser has been tested and confirmed experimentally. To complement our experimental observations, a comprehensive theoretical framework was formulated, with numerical simulations effectively corroborating the experimental measurements. The compelling agreement observed between our theoretical predictions and experimental data gives us confidence in the applicability of our developed theoretical model to predict future laser characteristics and behaviors. Therefore, we extended this numerical analysis to the range 1-5 GHz in order to identify the parameters that would make possible steady-state single pulse emission.

Funding. H2020 Marie Skłodowska-Curie Actions (872049); Generalitat Valenciana (ciprom/2022/30).

Acknowledgments. This work was supported in part by the European Union, project IPN-Bio (Ref.: H2020 Marie Skłodowska-Curie Actions 872049), and by the *Generalitat Valenciana* (Spain, Ref.: CIPROM/2022/30).

Disclosures. The authors declare no conflicts of interest.

Data availability. Data underlying the results presented in this paper are not publicly available at this time but may be obtained from the authors upon reasonable request.

References

1. J. K. Jang, M. Erkintalo, J. Schröder, *et al.*, “All-optical buffer based on temporal cavity solitons operating at 10 Gb/s,” *Opt. Lett.* **41**(19), 4526–4529 (2016).
2. T. Steinmetz, T. Wilken, C. Araujo-Hauck, *et al.*, “Laser frequency combs for astronomical observations,” *Science* **321**(5894), 1335–1337 (2008).
3. J. Na, J. C. Magee, and E. Betzig, “High-speed, low-photodamage nonlinear imaging using passive pulse splitters,” *Nat. Methods* **5**, 197–202 (2009).
4. S. T. Cundiff and A. M. Weiner, “Optical arbitrary waveform generation,” *Nat. Photonics* **4**(11), 760–766 (2010).
5. C. Kerse, H. Kalaycıoğlu, P. Elahi, *et al.*, “Ablation-cooled material removal with ultrafast bursts of pulses,” *Nature* **537**(7618), 84–88 (2016).
6. A. Bartels, D. Heinecke, and S. A. Diddams, “10-GHz self-referenced optical frequency comb,” *Science* **326**(5953), 681 (2009).
7. R. J. De Young and N. P. Barnes, “Profiling atmospheric water vapor using a fiber laser LIDAR system,” *Appl. Opt.* **49**(4), 562–567 (2010).
8. G. E. Villanueva, M. Ferri, and P. Perez-Millan, “Active and passive mode-locked fiber lasers for high-speed high-resolution photonic analog-to-digital conversion,” *IEEE J. Quantum Electron.* **48**(11), 1443–1452 (2012).
9. I. Mingareev, F. Weirauch, A. Olowinsky, *et al.*, “Welding of polymers using a 2 μm thulium fiber laser,” *Opt. Laser Technol.* **44**(7), 2095–2099 (2012).
10. W. Shen, J. Du, L. Sun, *et al.*, “Low-latency and high-speed hollow-core fiber optical interconnection at 2-micron waveband,” *J. Lightwave Technol.* **38**(15), 3874–3882 (2020).
11. P. Lin, T. Wang, W. Ma, *et al.*, “Transmission characteristics of 1.55 and 2.04 μm laser carriers in a simulated smoke channel based on an actively mode-locked fiber laser,” *Opt. Express* **28**(26), 39216–39226 (2020).
12. J. Qin, R. Dai, Y. Li, *et al.*, “20 GHz actively mode-locked thulium fiber laser,” *Opt. Express* **26**(20), 25769–25777 (2018).
13. Z.-C. Luo, M. Liu, H. Liu, *et al.*, “2 GHz passively harmonic mode-locked fiber laser by a microfiber-based topological insulator saturable absorber,” *Opt. Lett.* **38**(24), 5212–5215 (2013).
14. S. Sun, X. Shang, F. Yang, *et al.*, “Demonstration of high-stable self-mode-locking pulses based on self-focusing in fiber lasers,” *Infrared Phys. Technol.* **125**, 104244 (2022).
15. C. Cuadrado-Laborde, L. Tendela, E. Silvestre, *et al.*, “Build-up of different emission regimes in a nonlinear polarization rotation modelocked all-fiber laser,” *Chaos, Solitons & Fractals: X* **13**, 100114 (2024).
16. J. Szczepanek, T. M. Kardaś, M. Michalska, *et al.*, “Simple all-PM-fiber laser mode-locked with a nonlinear loop mirror,” *Opt. Lett.* **40**(15), 3500–3503 (2015).
17. A. E. Akosman and M. Y. Sander, “Low noise, mode-locked 253 MHz Tm/Ho fiber laser with core pumping at 790 nm,” *IEEE Photon. Technol. Lett.* **28**(17), 1878–1881 (2016).
18. P.-W. Kuan, K. Li, L. Zhang, *et al.*, “0.5-GHz repetition rate fundamentally Tm-doped mode-locked fiber laser,” *IEEE Photonics Technol. Lett.* **28**(14), 1525–1528 (2016).
19. J. Zeng, A. E. Akosman, and M. Y. Sander, “Scaling the repetition rate of thulium-doped ultrafast soliton fiber lasers to the GHz regime,” *Opt. Express* **26**(19), 24687–24694 (2018).
20. G. Tang, Z. Liang, W. Huang, *et al.*, “Broadband high-gain Tm³⁺/Ho³⁺ co-doped germanate glass multimaterial fiber for fiber lasers above 2 μm ,” *Opt. Express* **30**(18), 32693–32703 (2022).
21. G. Tang, Z. Liang, W. Huang, *et al.*, “4.3 GHz fundamental repetition rate passively mode-locked fiber laser using a silicate-clad heavily Tm³⁺-doped germanate core multimaterial fiber,” *Opt. Lett.* **47**(3), 682–685 (2022).

22. Z. Liang, W. Lin, W. Wang, *et al.*, “Low-noise mode-locking in a GHz repetition rate Tm³⁺-doped fiber laser,” *Opt. Lett.* **49**(2), 403–406 (2024).
23. Z. Liang, W. Lin, J. Wu, *et al.*, “>10 GHz femtosecond fiber laser system at 2.0 μm,” *Opt. Lett.* **47**(7), 1867–1870 (2022).
24. Z. Liang, M. Pan, W. Lin, *et al.*, “All-fiber GHz few-cycle pulse generation at 2 μm,” *Opt. Lett.* **49**(19), 5356–5359 (2024).
25. H. Cheng, W. Lin, T. Qiao, *et al.*, “Theoretical and experimental analysis of instability of continuous wave mode locking: Towards high fundamental repetition rate in Tm³⁺-doped fiber lasers,” *Opt. Express* **24**(26), 29882–29895 (2016).
26. C. Cuadrado-Laborde, H. Muñoz-Marco, P. Pérez-Millán, *et al.*, “1 GHz fundamental repetition rate thulium-doped all-polarization maintaining modelocked fiber laser,” *J. Phys. Photonics* **7**(1), 015001 (2025).
27. Y.-W. Lee, H.-W. Chien, C.-H. Cho, *et al.*, “Heavily Tm³⁺-doped silicate fiber for high-gain fiber amplifiers,” *Fibers* **1**(3), 82–92 (2013).
28. Bathop GmbH, SAM - 2000nm. (2024, February 29). <https://www.batop.de/products/saturable-absorber/saturable-absorber-mirror/saturable-absorber-mirror-2000nm.html>
29. J. Sotor, J. Boguslawski, T. Martynkien, *et al.*, “All-polarization-maintaining, stretched-pulse Tm-doped fiber laser, mode-locked by a graphene saturable absorber,” *Opt. Lett.* **42**(8), 1592–1595 (2017).
30. C. Cuadrado-Laborde, A. Díez, J. L. Cruz, *et al.*, “Long- and short-term stability of all polarization-maintaining thulium doped passively mode-locked fiber lasers with emission wavelengths at 1.95 μm and 2.07 μm,” *Appl. Sci.* **13**(3), 1981 (2023).
31. C. Cuadrado-Laborde, A. Carrascosa, P. Pérez-Millán, *et al.*, “Phase recovery by using optical fiber dispersion,” *Opt. Lett.* **39**(3), 598–601 (2014).
32. P. Hlubina, “White-light spectral interferometry with the uncompensated Michelson interferometer and the group refractive index dispersion in fused silica,” *Opt. Commun.* **193**(1-6), 1–7 (2001).
33. A. E. Siegman, *Lasers*, University Science Books, 1986.
34. P. Lazaridis, G. Debarge, and P. Gallion, “Time–bandwidth product of chirped sech² pulses: application to phase–amplitude-coupling factor measurement,” *Opt. Lett.* **20**(10), 1160–1162 (1995).
35. G. P. Agrawal, *Nonlinear Fiber Optics*, 4th Ed. (Academic Press, 2007).
36. X. Zhang, F. Li, K. Nakkeeran, *et al.*, “Impact of spectral filtering on multipulsing instability in mode-locked fiber lasers,” *IEEE J. Select. Topics Quantum Electron.* **24**(3), 1 (2018).
37. G. P. Agrawal, *Applications of nonlinear fiber optics*, 2nd ed. (Academic Press, 2007).
38. M. Haiml, R. Grange, and U. Keller, “Optical characterization of semiconductor saturable absorbers,” *Appl. Phys. B* **79**(3), 331–339 (2004).
39. T. Schibli, E. Thoen, F. Kärtner, *et al.*, “Suppression of Q-switched mode locking and break-up into multiple pulses by inverse saturable absorption,” *Appl. Phys. B:Lasers Opt.* **70**(Suppl. S1), S41–S49 (2000).
40. T. R. Taha and X. Xu, “Parallel split-step Fourier methods for the coupled nonlinear Schrödinger type equations,” *J. Supercomput.* **32**(1), 5–23 (2005).
41. J. A. C. Weideman and B. M. Herbst, “Split-step methods for the solution of the nonlinear Schrödinger equation,” *SIAM J. Numer. Anal.* **23**(3), 485–507 (1986).
42. M. E. Fermann, M. J. Andrejco, M. L. Stock, *et al.*, “Passive mode locking in erbium fiber lasers with negative group delay,” *Appl. Phys. Lett.* **62**(9), 910–912 (1993).
43. H. A. Haus, “Mode-locking of lasers,” *IEEE J. Select. Topics Quantum Electron.* **6**(6), 1173–1185 (2000).
44. O. E. Martinez, R. L. Fork, and J. P. Gordon, “Theory of passively mode-locked lasers including self-phase modulation and group-velocity dispersion,” *Opt. Lett.* **9**(5), 156–158 (1984).